THE JOURNAL OF PHYSICAL CHEMISTRY C
A JOURNAL OF THE AMERICAN CHEMICAL SOCIETY

pubs.acs.org/JPCC

Article

Unexpected Superparamagnetic Behavior in Nanocrystalline Niobium-Based High-Entropy Alloys

Debabrata Das, Yohannes Getahun, Francelia Sanchez Escobar, Rebecca Romero, Ahmed A. El-Gendy,* and C. V. Ramana*

Cite This: *J. Phys. Chem. C* 2022, 126, 14255−14263

Read Online

ACCESS | Metrics & More | Article Recommendations | Supporting Information

ABSTRACT: Herein, we report on the evolution of superparamagnetic behavior of Nb−Cr−Ta−V−W refractory high entropy alloy (RHEA) nanoparticles synthesized by a facile mechanical pulverization (high-energy ball milling) technique. Detailed X-ray diffraction (XRD), scanning electron microscopy (SEM), and energy-dispersive X-ray spectroscopy (EDS) analyses have been made to evaluate the structure, morphology, compositional, and elemental distribution characteristics of RHEA nanoparticles and further compared with the bulk. XRD and SEM data coupled with EDS analyses indicate that the nano-RHEA retains the parent crystal structure and phase, but the size dramatically decreases with milling time. The average crystallite size decreases from ∼32 to ∼12 nm with an increasing milling time to 16 h. While the bulk samples exhibit diamagnetic behavior, interestingly, RHEA nanoparticles demonstrate superparamagnetic nature. Magnetic measurements, in both room temperature and cryogenic conditions, provide evidence of the temperature-independent superparamagnetic nature of the RHEA nanoparticles. Furthermore, the saturation magnetization value exponentially increased with milling time and stabilized after 8 h of pulverization, whereas the magnetic domain size followed an opposite trend. We believe drastic reduction in the magnetic domain size is responsible for this unusual and unexpected superparamagnetic pattern of the RHEA nanoparticle, which opens up a new route for low-cost magnetic applications under harsh environment conditions.

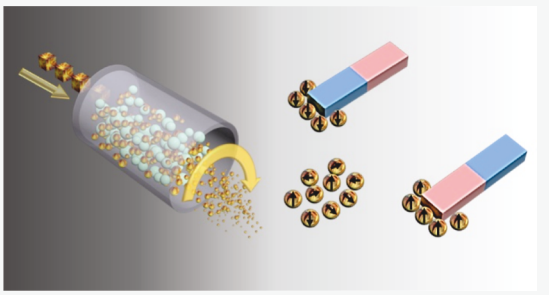

INTRODUCTION

Since prehistoric times, human civilization continuously and steadily looked for new materials with multidimensional functionality and diverse applications. A common strategy that can be noted was mixing and alloying of different metals to exploit their unique characteristics and fabricating new composites with superior functionality and device applicability.[1−4] Initially, the strategy was to incorporate a secondary material into the host system and tailor its functionality, such as melting point, hardness, elasticity, corrosion resistance, and so forth.[1−4] However, with the scientific advancements made over many years and decades, this approach has become more precise and sophisticated. Scientists and engineers explored many possible ways to design materials, especially the complex alloys, by selectively spanning the search and/or mixing metals available across the periodic table.[5,6] In the series of evolution, the most recent attention is toward the high entropy alloys (HEAs) or multiprincipal element alloys (MPEAs), which can fulfil the requirements of future energy, aerospace, and nuclear technologies.[5−9] The HEAs/MPEAs were first reported at the dawn of the current century.[5,6,10,11] On the contrary, with the conventional alloy system, where a small portion of the host material is substituted by secondary elements, the HEA belongs to an equimolar or near equimolar mixture of various elemental metals.[10,11] In the entropy contour plot, conventional alloys belong to corners, whereas the HEA overtakes the central region.[12] By definition (composition-based), the HEA should have at least five or more principal elements.[12−14] Percentage of each component may vary depending on its characteristic evolution. Whereas entropy-based definition demands a cumulative entropy of the overall mixture above a certain limit. During the initial stages, HEAs were mainly considered for four unique characteristics, such as a higher aggregated entropy, slower diffusion, acute lattice distortion, and finally, the cocktail effect.[12−17] With progressive research in this field, the overall optimization strategy has been tailored to some extent, depending on specific applications.

The concept of HEA was initially limited to only metallic materials or alloys. However, it has been continuously evolving to explore new compounds, such as oxide-, carbide-, and nitride-based materials, with extended technological application in many diverse fields.[18,19] For metal-based HEA preparation, standard metallurgical approaches, such as

Received: May 5, 2022
Revised: August 2, 2022
Published: August 12, 2022

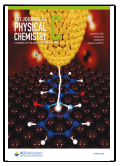

resistance melting, arc melting, induction melting, rapid solidification, mechanical alloying, and powder metallurgy, were utilized. The resulting alloy might be either in the amorphous or in crystalline phase. Most of the efforts reported a BCC (body-centered cubic) or FCC (face-centered cubic) lattice system in addition to a few HCP (hexagonal close packed) configurations.[10,11] Depending on the fabrication process and primary elements, there might be a probability of defect formation, such as random nucleation of mesophases inside the host alloy, amorphous mixed phase formation, microstructure initiation, and so on. In recent years, especially with the success seen in bulk of the alloys, several other physical and chemical methods, such as sputtering, thermal evaporation, chemical synthesis, chemical vapor deposition, nanostructure synthesis, pyrolysis, and so on, were also explored to realize nanostructured HEAs with unique structural characteristics and stability.[10,11,19−24] For instance, Zou et al. reported that nanocrystalline refractory HEA (RHEA) micropillars have a superior structure−strength/stability property, even at an elevated temperature.[24] Outstanding creep resistance at a higher temperature opens up a new domain of nanocrystalline RHEA for extreme environment applications, particularly those in the aerospace, defense, and energy sector. An oriented HEA nitride film was demonstrated by Shu et al. through controlled ion energy manipulation during sputtering at 400 °C with an increasing substrate potential.[19] While the substrate biasing was increased from 0 to −130 V, there was a clear modulation from polycrystalline FFC planes to a highly ordered (002) orientation with a lower surface roughness and higher hardness value until 28.0 GPa. Realizing the potential of nanostructured HEAs, the scientific and engineering research community considered designing more advanced, nanoscale HEAs for multifunctional device applications.

In recent years, considerable attention has been directed toward the RHEA, which is based on various combinations of refractory metals, such as Nb, Ta, Hf, Ti, Zr, Mo, Cr, V, and W.[25−27] Senkov et al. first introduced the RHEAs and extensively investigated various compositions. Owing to an extremely high melting point, the most successful application of RHEAs is for high-temperature use.[25−27] However, other applications or application of RHEAs, especially at the nanoscale dimensions, to other domains is yet to be explored. Although there are few efforts that report the controlled growth and microstructure of nanostructured HEAs, demonstrating HEA nanoparticles with ultra-narrow size distribution along with enhanced functionality is challenging. Gao et al. have successfully manifested HEA nanoparticles, having a uniform size distribution with up to 10 elemental components (MnCoNiCuRhPdSnIrPtAu), on various platforms using the fast-moving bed pyrolysis method.[21] Simultaneous pyrolysis of the precursor at an elevated temperature, to achieve supersaturation growth condition along with smaller nucleation centers, has produced this uniform HEA nanoparticle size distribution, which evinced batter stability as an active electrode for electrochemical hydrogen evolution. Qiao et al. suggested a facile microwave-assisted fast-heating technique to fabricate uniformly distributed scalable PtPdFeCoNi HEA nanoparticles on carbonized wood and carbon nanofiber, which can be adopted in the roll-to-roll process for rapid prototyping of advanced multifunctional coatings.[22] To investigate the core elemental shifting of such a multielemental alloy system, Xu et al. used a novel carbothermal shock method to stabilize HEA nanoparticles on carbon nanofibers, followed by X-ray photoelectron spectroscopy.[23] Here, in this work, we focus our attention on the nanoscale synthesis and unusual magnetic behavior in Nb-based refractory alloys, which might open new avenues in the topical area of materials for extreme environment applications. The field of superparamagnetism is evolving gradually for advanced sensing applications and can potentially welcome new materials.

Under the enlightenment of the above brief discussion, it is clear that scientific advancement on the HEA and related oxide−nitride material system is at its dawn. In this context, we propose a facile method based on the mechanical high-energy ball-milling technique to fabricate scalable Nb−Cr−Ta−V−W RHEA nanoparticles with superior resistivity under high-temperature oxidation. The specific composition was based on our previous study, as reported elsewhere. We present a detailed investigation of the structure, morphology, chemical composition, and elemental distribution characteristics of the Nb-based RHEA nanoparticles, which convincingly present a surprising and unexpected superparamagnetic behavior, while the bulk or any other metal involved does not show or expect to show such behavior. We believe that, during the mechanical pulverization processes, kinetic energy was transferred into the host crystal to disrupt into smaller particles. Also, assertively, the drastic reduction in the overall crystallite size promotes the nucleation of even smaller magnetic domains, which, in turn, promotes superparamagnetism over a broad temperature range.

MATERIALS AND METHODS

Nanoparticle Synthesis—Ball Milling. The as-received HEA samples were prepared by the vacuum arc melting process. The high-energy ball milling experiments were performed using an 8000M Mixer/Mill by SPEX Sample Prep, as shown in Figure 1. The as-made bulk alloy was

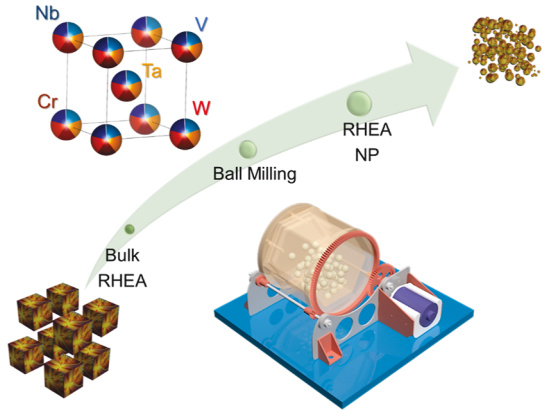

Figure 1. Scheme of the system and the synthesis/fabrication of the Nb−Cr−Ta−V−W RHEA.

grounded by mortar and pestle, and then the powder was sealed with hexane solution and stainless-steel balls in a stainless-steel jar. The sample was milled for 2, 4, 8, and 16 h.

X-ray Diffraction. A Rigaku SmartLab diffractometer, equipped with a 2D hybrid pixel array detector (HPAD), was employed for X-ray diffraction (XRD) analysis. A trace amount of the Nb−Cr−Ta−V−W RHEA nanoparticle powder was placed on a zero-diffraction plate to eliminate any diffraction peak from the sample stage. The diffraction data

https://doi.org/10.1021/acs.jpcc.2c03111
J. Phys. Chem. C 2022, 126, 14255−14263

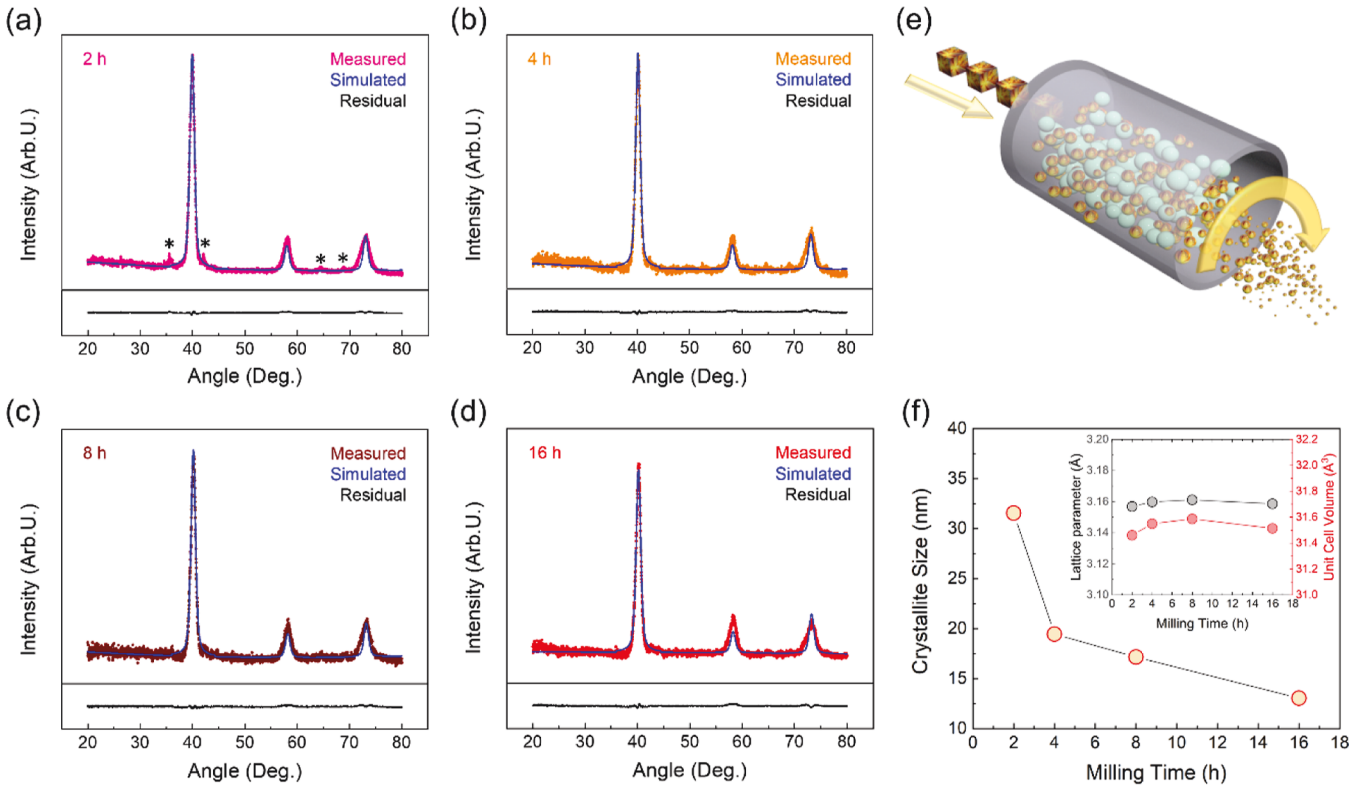

Figure 2. (a–d) Measured and refined XRD data of pulverized RHEA samples with increasing ball-milling time. (e) Schematic of the high-power mechanical grinding process to prepare RHEA nanoparticles. (f) Evolution of the crystallite size with increasing mechanical pulverization time. The inset shows the variation in the lattice parameter and unit cell volume with increasing milling time.

were analyzed with HighScore Plus software to extract crystallographic information of RHEA nanoparticles.[28−30]

Scanning Electron Microscopy. The Nb−Cr−Ta−V−W RHEA nanoparticle samples were used to investigate the topographical characteristics using an FEI Magellan 400 scanning electron microscope. The nanoparticle samples were mounted on carbon conducting tape for better resolution. The accelerating voltage was kept to 5 kV.[30]

Energy-Dispersive X-ray Spectroscopy. To apprehend the phase separation, elemental distribution, and mixed composition chemistry, we performed energy dispersive X-ray spectroscopy (EDS) measurements on Nb−Cr−Ta−V−W RHEA nanoparticle samples. The elemental analysis was performed using EDS with the use of X-ray color mapping to approximately determine the elements present and spatial distribution characteristics.[30]

Magnetic Measurements. To characterize the observed magnetic properties of the samples, we used a vibrating sample magnetometer (VersaLab) by Quantum design.[31] We measured the magnetic properties of the samples under an applied magnetic field range from 3 to −3 T at temperatures of 300 and 50 K.

RESULTS AND DISCUSSION

Crystallography. Figure 2a−d shows the XRD patterns of HEA nanocrystalline samples. All the data were analyzed to determine the crystal structure and phase. Additionally, refinement the XRD data was done using X'pert HighScore plus software. The Rietveld refinement values were determined with a low goodness of fit below 3, which makes these calculations very dependable.[30] The pseudo-Voigt peak profile was used to fit the observed XRD patterns. The experimental and refinement XRD data indicate that the elements of the HEA conform into a body-centered cubic structure. However, as can be seen Figure 2a−d and since the metal atoms considerably vary in size, the X-ray diffraction peaks tend to be broader without any segregation into individual phases. Furthermore, the refinement data for all the samples do not match with any unintentional impurities or any of the Cr-based complex magnetic alloys. It shows a purely Nb−Cr−Ta−V−W-based solid solution, having a BCC crystal structure. The most dominant peaks, approximately at 39, 58, and 73°, were recognized as (110), (200), and (211) crystal planes. Earlier Senkov et al. have reported a similar crystallographic nature of CrNbTiVZr and NbMoTaW bulk RHEAs.[27,32] Predominantly, all of them are a BCC crystal structure, the same as the host metals. However, preferential orientations, specifically in three different directions (110, 200, 211), are due to the cumulative effect of the solid solution. We believe these orientations correspond with the lowest-possible formation energies. Parallelly, there exists few low intensity peaks (marked as * in Figure 2a), which disappear gradually with higher milling time. Probably, some low-density complex metallic clusters are responsible for these peaks and slowly dissociate with a prolonged mechanical grinding process. The XRD peaks for HEA nanocrystalline samples indicate the broader nature, corresponding to every crystal orientation, which is due to the multicomponent solid solution of corresponding HEA and size reduction with increasing time. In order to compare the XRD pattern of pulverized samples with the bulk crystal, Figure S1 presents the as-received bulk Nb−Cr−Ta−V−W HEA XRD data. The similarity of the nano-RHEA and bulk samples is evident.

https://doi.org/10.1021/acs.jpcc.2c03111
J. Phys. Chem. C 2022, 126, 14255−14263

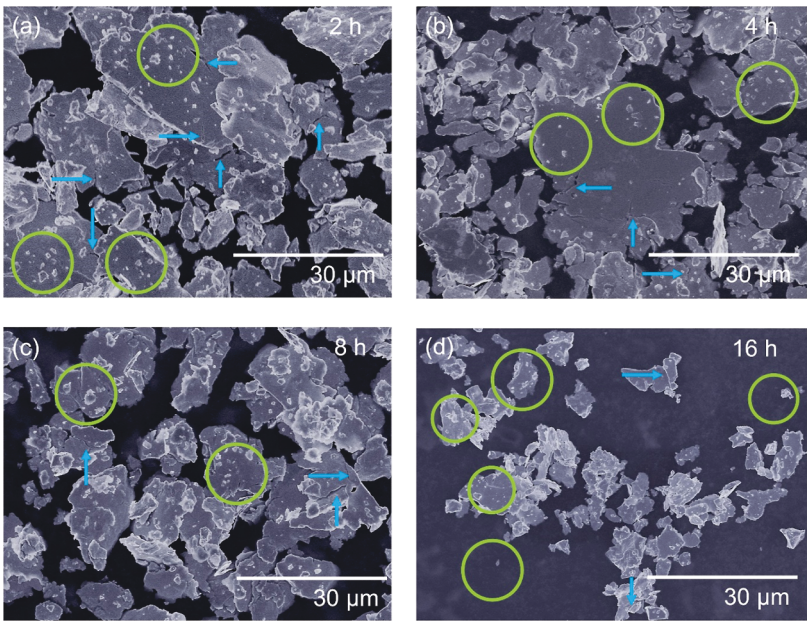

Figure 3. Low-magnification scanning electron microscope images of samples pulverized for 2 h (a), 4 h (b), 8 h (c), and 16 h (d) duration, respectively.

The XRD data were further analyzed to evaluate the tailoring of the intrinsic crystallite size of the as-prepared samples. We have used the Scherrer equation to calculate the modulation of the crystallite size with increasing grinding time. Figure 2f shows a gradual reduction in the average crystallite size with increasing pulverization, whereas there is not any significant change in the lattice parameter and unit cell volume (inset of Figure 2f). The bulk RHEA was subjected to prolonged milling, where mechanical energy was transferred into the crystallite sites to rapture the same and form smaller particles without any significant change in the unit cell. With increasing processing time, the overall material was subjected to more energy and formed higher density RHEA nanoparticles. Figure 2e depicts a schematic of the high-energy ball milling process, where bulk RHEA samples go through a mechanical pulverization process and are finally converted into a fine powder of nanoparticles.

Morphology and Microstructure. Figure 3 shows low-magnification evidence of surface morphology evolution with increasing milling time. As shown in Figure 3a, the shortest grinding period (2 h) has resulted in larger macroparticles. The remarkable feature, which is evident from these micrographs (Figure 3a–d), is the fact that, with increasing time duration, there is a gradual reduction in the particle size. It is worthwhile to identify and consider the size distribution as a function of time. For every sample, both micro- and nanoparticles coexist; however, with an increasing grinding period, the density of particles with nanodimension increases. To illustratively represent the process, some of these are identified with green circles, as illustrative of nanoparticle HEAs in Figure 3a–d. This is a typical behavior of the mechanical pulverization process. Assertively, the grinding with stainless-steel spheres breaks down the active HEA material. The higher amount of collision with the active material resulted in even smaller particle formation. With a visual inspection, it is evident that processed samples show non-Gaussian size distribution within a broad length scale. Owing to partial or absolute spatial overlapping of micro- and nanoparticles, calculation of actual size distribution is not possible in this case. Though we have confirmed the tentative particle size variation by imaging at various spots, these images have been shown as representative evidence of the corresponding size variation. The shape of the final particles, after grinding, is irregular in shape and carries evidence of mechanical pulverization, such as cleaved facets at the junction between two broken particles. Also, the evidence of primary crack formation is clearly visible in every sample and reduces as the host material gradually raptures into smaller particles with increasing milling time. These are shown with blue arrow marks in Figure 3a–d. As a comparison with the RHEA nanoparticles, the SEM image of the polished bulk sample is also included in the Supporting Information (Figure S2). Five different phases with varying alloy compositions have been observed, which was published earlier.[8,9]

For detailed topographical analysis on the nanometer scale, we have also shown high-magnification images in Figure 4. Samples with increasing milling time are shown in Figure 4a–d. Few representative macro- and nanoparticles are identified with white and green circles, respectively. Particles with both dimension ranges are present in all of the samples, but macroparticles show a gradual reduction in the length scale with increasing grinding time. In samples with 2 and 4 h milling time, there is evidence of mechanical crack formation (shown with blue arrows). Those spots are potential positions from where HEA particles might break down and form smaller particles. Also, there is evidence of cleaved facets in the micro–nano particles after peeling off from the host material. Yellow arrows have been used to identify few such spots in Figure 4b,c. To get an idea about the nanoparticle size, we have even shown higher resolution images in Figure 4e,f. The smallest possible particle size is observed as ∼69 nm while measuring the dimension diagonally (see Figure 4f).

Elemental Composition and Distribution. We examined both the bulk of the alloy and nanomaterials synthesized to understand the chemical composition changes (if any) as a result of nanoscale materials processing. The microstructure of the as-received Cr–Nb–Ta–V–W HEA is shown in Figures

https://doi.org/10.1021/acs.jpcc.2c03111
J. Phys. Chem. C 2022, 126, 14255–14263

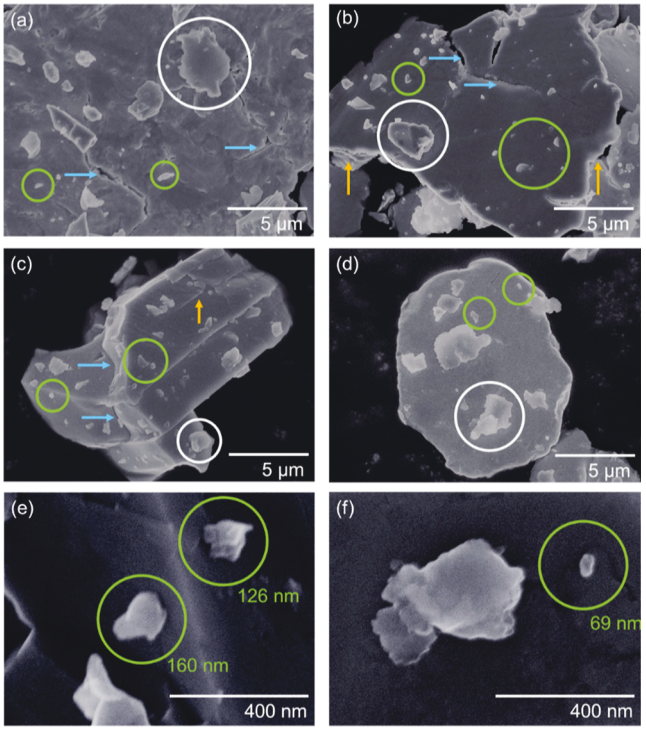

Figure 4. High-magnification scanning electron microscope images of samples pulverized for 2 h (a), 4 h (b), 8 h (c), and 16 h (d) duration, respectively. Figure (e) and (f) shows nanoparticles with the lowest possible dimension measured.

S2 and S3. The map sum spectrum presents a nearly equiatomic structure (Table S1). It can be seen that, although the W content is slightly higher than the other constituent elements, the composition of the alloy is uniform. However, slightly higher W content may be due to the large area of the W-rich phase shown in the captured area. Five different phases, identified earlier, were verified in this study.[8,9] All of the phases are marked in Figure S3a. The first phase, a W-rich phase, is the largest phase present, with one of the larger grains being highlighted in the enlarged area. Though the W content of the area marked in the figure is not as high as first reported,[8,9] it is still predominantly W at nearly 83 at. %, with only trace amounts of Cr, Ta, and V. No Nb content was identified in this area of phase 1. The second phase, marked as area 2 on the figure, is a V-rich phase with a dark, cloudy appearance. The phase contains trace amounts of W and moderate amounts of Cr, Nb, and Ta. The third phase is a distinct dark gray structure that is Cr-rich with moderate amounts of Nb, Ta, V, and W. The fourth phase is the counterpart of the second phase, which is an Nb-rich phase having an analogous cloudy appearance but lighter in color than phase 2. The fifth phase is a darker, grainier area that was identified as the Laves phase Ta_2V. This phase is nearly depleted of W and contains only trace amounts of Cr and Nb. The EDS mapping highlights the areas in which the elements are rich in concentration and provides comparable results to those first identified.[8,9]

Having established the chemical homogeneity of the bulk sample, which was used as a precursor to producing nanoscale alloys, we now turn our attention to the microstructure and chemical analyses of the samples produced as a function of milling time. A larger, macro view of the micro/nanoparticles is presented in Figure 5a. As shown in the color mapping (Figure 5b–f), the constituent elements are uniformly distributed across various particles and continue to provide an equiatomic composition, as indicated by the map summation of the EDS spectrum. Each constituent element has bright areas on its respective color map, indicating that these may be areas that relate to its enriched phase described above. This relatively uniform distribution indicates that there were no significant microstructural changes in the alloy subjected to deformation induced by the milling. The percentage of each element is summarized in Table 1.

Table 1. Chemical Composition Distribution of RHEA Nanoparticles Shown in Figure 4

element	map sum nanoparticle (%)
Cr	20.1
Nb	22.3
Ta	18.8
V	19.7
W	19.0

Upon further investigation of the samples produced under various milling times, Figure 6 shows the EDS color mapping and map sum of each respective spectrum (2 h (Figure 6a–f) and 16 h (Figure 6g–l) ball milling, respectively). All the samples produced under increasing milling times do not show significant changes in the composition of the alloy, remaining nearly equiatomic in terms of chemical composition. Table 2 depicts the percentage composition of the lowest and the

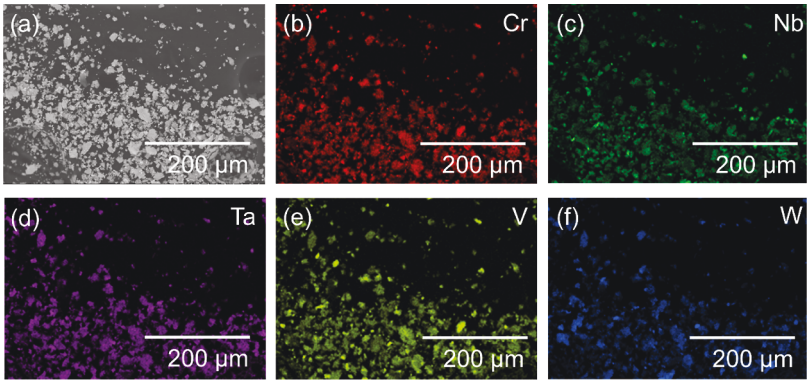

Figure 5. Low-magnification SEM–EDX color mapping of RHEA nanoparticles with 2 h grinding time. Figure (a) shows the size distribution, whereas figure (b–f) shows the chemical distribution of RHEA elements.

https://doi.org/10.1021/acs.jpcc.2c03111
J. Phys. Chem. C 2022, 126, 14255–14263

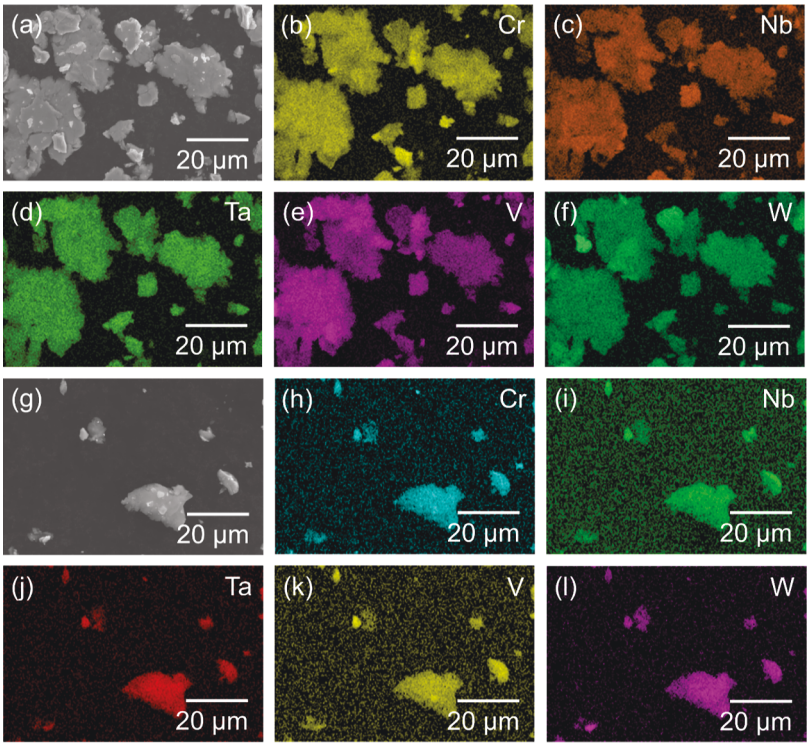

Figure 6. Figure (a) and (g) shows the high-resolution morphological size distribution of 2 h and 16 h pulverized samples. Figure (b–f) and (h–l) depicts the elemental distribution of RHEA nanoparticles in corresponding samples.

Table 2. Chemical Composition Distribution RHEA Nanoparticles Shown in Figure 5

element	map sum (%) 2 h	map sum (%) 16 h
Cr	22.1	16.7
Nb	20.8	28.8
Ta	20.0	22.4
V	21.2	14.5
W	16.0	17.6

highest ball milling samples. However, while the overall macroregions of the samples are homogeneous, the minor variations deviating from 100% equiatomic can be assumed that it may be related to the type of particle captured in the image area, potentially containing a particle of a phase of one of the enriched elements. Because there is no trend in any of the element concentrations increasing or decreasing, it is believed that the alloy retained its composition and microstructure despite the change in milling time in the processing of these nanoscale materials.

Magnetic Properties. Although we did not observe any significant changes in the microstructure and chemical composition of the samples with increasing milling time, there was a drastic change in the magnetic behavior of RHEA nanoparticles. The samples, after mechanical pulverization, became magnetic and showed an attractive force to the permanent magnet. Figure 6 displays the magnetic behavior of bulk and 2 h ball-milled samples, revealing no magnetic attractive force for the RHEA cube (Figure 7a), while the nanoparticles show an attractive force to the magnet (Figure 7b).

Therefore, in order to confirm the magnetic behavior, we measured the magnetic properties of the bulk (0 h) and ball-milled (2, 4, 8, and 16 h) samples up to 3 T at room

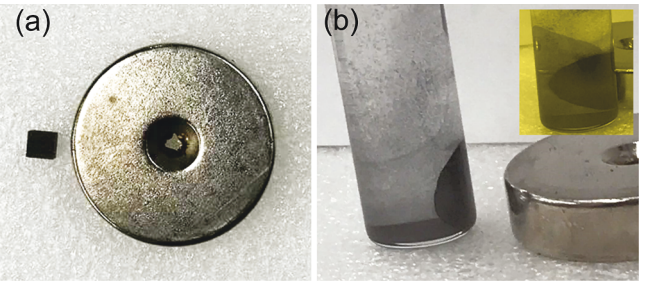

Figure 7. Magnetic response of bulk (a) and prolonged ball-milled (b) samples to the permanent magnet.

temperature (300 K) and cryogenic temperature (50 K). In Figure 8a,b, the magnetization dependence on the external magnetic field is measured at 300 and 50 K, revealing diamagnetic behavior for the bulk (0 h) and superparamagnetic behaviors for all the ball-milled samples. The ball-milled samples reveal coercivity (HC) close to zero and saturation magnetization (MS) of 5, 6, 7, and 7 emu/g for the samples milled at 2, 4, 8, and 16 h, respectively. To confirm these observations, the magnetic domain size has been determined by evaluating the initial slopes of the M versus H curves at 300 K.[33] While the domain size of the bulk sample is microscopic in size, around 1000–100 000 nm,[34] the analysis yields a magnetic domain size of 17, 15, 13, and 14 nm for the ball-milled samples at 2, 4, 8, and 16 h, respectively. The saturation magnetization, as well as magnetic domain size dependence on ball milling time and domain, is plotted, as shown in Figure 8c. The saturation magnetization and magnetic domain size exponentially increase and decrease, respectively, then saturate at a higher milling time of 8 and 16 h. The change in the magnetic domain size from the bulk of 1000 nm to ball-milled samples with few tens of nanometers is

https://doi.org/10.1021/acs.jpcc.2c03111
J. Phys. Chem. C 2022, 126, 14255–14263

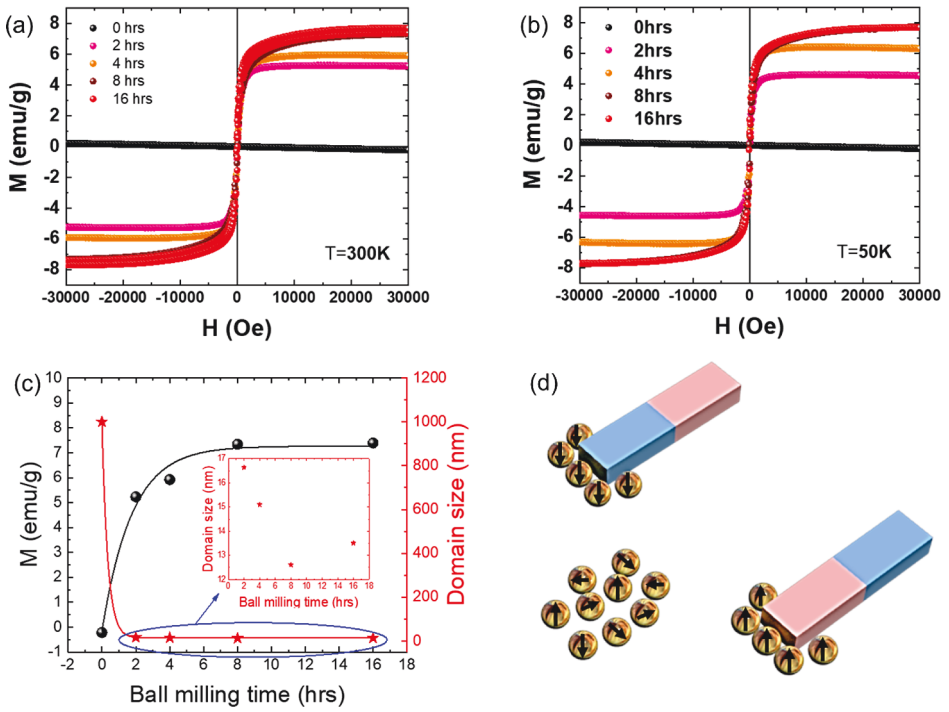

Figure 8. Magnetization dependence on the magnetic field at (a) 300 K and (b) 50 K. (C) Ball milling time dependence on saturation magnetization and the magnetic domain size of the samples. (d) Schematic of superparamagnetic RHEA nanoparticles under the influence of permanent magnets.

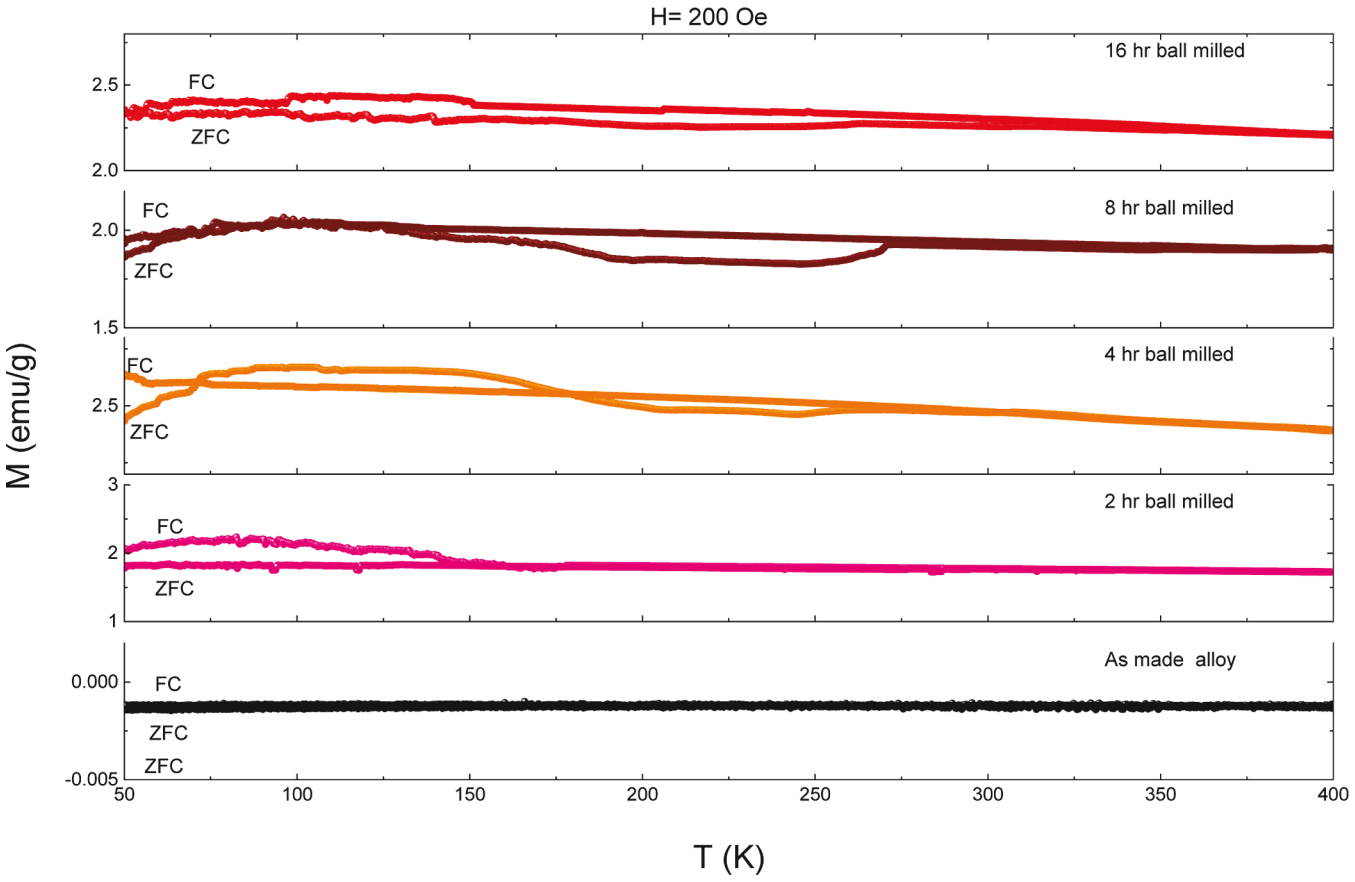

Figure 9. Magnetization dependence on temperature at 200 Oe for the as-made 2, 4, 8, and 16 h ball-milled alloys.

responsible for the observed unexpected superparamagnetic behavior, as well as the magnetic attractive force of the ball-milled samples to the magnet. Figure 8d shows a schematic of how the RHEA nanoparticles are changing the magnetic

https://doi.org/10.1021/acs.jpcc.2c03111
J. Phys. Chem. C 2022, 126, 14255−14263

orientation with different magnetic polarities, whereas they show random orientation without any significant external magnetic field. These outstanding findings reveal new routes for adding a new magnetic property of HEAs by reducing the domain size to the nanoscale.

In order to verify the superparamagnetic behavior of the nanoscaled samples and the nonmagnetic properties of the bulk sample, magnetization dependence on temperature ($M \times T$) at a constant magnetic field of 200 Oe has been measured in the range of 50−400 K, as shown in Figure 9. As seen in Figure 9, the zero field cooled (ZFC) and FC curves are coincident from 50 to 400 K, revealing that the blocking temperature (T_B), which is the characteristic feature of superparamagnetic behavior, is below 50, 85, 96, and 125 K for ball-milled samples at 2, 4, 8, and 16 h, respectively. This confirms the observed superparamagnetic behavior of the nanoscaled samples at room temperature and at 50 K. The ZFC/FC curve of the as-made bulk materials shows below zero magnetization from 50 to 400 K under an applied magnetic field of 200 Oe, confirming the nonmagnetic behavior of the bulk sample.

SUMMARY AND CONCLUSIONS

Unexpected superparamagnetic behavior was observed in RHEA nanoparticles, which is different from their bulk counterpart. From phase structure measurements by XRD, we did not observe any significant change in the crystalline structure between the bulk and the nanoscale RHEA samples. However, we observed a significant change in the magnetic domain size between the bulk and the nanoscaled samples. The reduction in the magnetic domain size is responsible for such superparamagnetic behavior of the nanoscaled samples. Magnetic measurements in both room temperature and cryogenic conditions with a closed hysteresis loop ($M \times H$) confirm the superparamagnetic behavior of the RHEA nanoparticles. The $M \times T$ data confirm the $M \times H$ results of the observed superparamagnetic behavior of the nanoscaled samples and the nonmagnetic behavior of the bulk sample. Therefore, these outstanding unexpected magnetic behaviors open new routes for RHEA's potential for low-cost magnetic applications under harsh environmental conditions.

ASSOCIATED CONTENT

Supporting Information

The Supporting Information is available free of charge at https://pubs.acs.org/doi/10.1021/acs.jpcc.2c03111.

Structural, morphological, and chemical composition of bulk RHEA samples (PDF)

AUTHOR INFORMATION

Corresponding Authors

Ahmed A. El-Gendy − *Department of Physics, University of Texas at El Paso, El Paso, Texas 79968, United States;* orcid.org/0000-0001-7212-6647; Email: aelgendy@utep.edu

C. V. Ramana − *Centre for Advanced Materials Research (CMR), University of Texas at El Paso, El Paso, Texas 79968, United States; Department of Mechanical Engineering, University of Texas at El Paso, El Paso, Texas 79968, United States;* orcid.org/0000-0002-5286-3065; Email: rvchintalapalle@utep.edu

Authors

Debabrata Das − *Centre for Advanced Materials Research (CMR), University of Texas at El Paso, El Paso, Texas 79968, United States;* orcid.org/0000-0003-4326-6805

Yohannes Getahun − *Department of Environmental Science and Engineering and Department of Physics, University of Texas at El Paso, El Paso, Texas 79968, United States*

Francelia Sanchez Escobar − *Centre for Advanced Materials Research (CMR), University of Texas at El Paso, El Paso, Texas 79968, United States; Department of Metallurgical, Materials, and Biomedical Engineering, University of Texas at El Paso, El Paso, Texas 79968, United States*

Rebecca Romero − *Centre for Advanced Materials Research (CMR), University of Texas at El Paso, El Paso, Texas 79968, United States; Department of Metallurgical, Materials, and Biomedical Engineering, University of Texas at El Paso, El Paso, Texas 79968, United States*

Complete contact information is available at: https://pubs.acs.org/10.1021/acs.jpcc.2c03111

Notes

The authors declare no competing financial interest.

ACKNOWLEDGMENTS

The authors acknowledge, with pleasure, the support from the National Science Foundation (NSF) with grant #2009358 and NSF-PREM grant #DMR-1827745. A.A.E. acknowledges the Startup and Rising Stars funds by UTEP and UT System, respectively.

REFERENCES

(1) Greeley, J.; Mavrikakis, M. Surface and Subsurface Hydrogen: Adsorption Properties on Transition Metals and Near-Surface Alloys. *J. Phys. Chem. B* **2005**, *109*, 3460−3471.

(2) Lee, S.; Hoffmann, R. Bcc and Fcc Transition Metals and Alloys: A Central Role for the Jahn-Teller Effect in Explaining Their Ideal and Distorted Structures. *J. Am. Chem. Soc.* **2002**, *124*, 4811−4823.

(3) Liz-Marzân, L. M. Tailoring Surface Plasmons through the Morphology and Assembly of Metal Nanoparticles. *Langmuir* **2006**, *22*, 32−41.

(4) Stamenkovic, V. R.; Mun, B. S.; Mayrhofer, K. J. J.; Ross, P. N.; Markovic, N. M. Effect of Surface Composition on Electronic Structure, Stability, and Electrocatalytic Properties of Pt-Transition Metal Alloys: Pt-Skin versus Pt-Skeleton Surfaces. *J. Am. Chem. Soc.* **2006**, *128*, 8813−8819.

(5) Yeh, J.-W.; Chen, S.-K.; Lin, S.-J.; Gan, J.-Y.; Chin, T.-S.; Shun, T.-T.; Tsau, C.-H.; Chang, S.-Y. Nanostructured High-Entropy Alloys with Multiple Principal Elements Novel Alloy Design. *Adv. Eng. Mater.* **2004**, *6*, 299−303.

(6) Yeh, J.-W.; Lin, S.-K.; Chin, J.-Y.; Gan, S.-J.; Chen, T.-S.; Shun, T.-T.; Tsau, C.-H.; Chou, S.-Y. Formation of Simple Crystal Structures in Cu-Co-Ni-Cr-Al-Fe-Ti-V Alloys with Multiprincipal Metallic Elements. *Metall. Mater. Trans. A* **2004**, *35*, 2533−2536.

(7) Romero, R.; Makeswaran, N.; Naraparaju, R.; Ramana, C. V. Examination of the Oxidation and Metal−Oxide Layer Interface of a Cr−Nb−Ta−V−W High Entropy Alloy at Elevated Temperatures. *Adv. Eng. Mater.* **2021**, *23*, 2100164.

(8) Varma, S. K.; Sanchez, F.; Ramana, C. V. Microstructures in a Nb-Cr-V-W-Ta high entropy alloy during annealing. *J. Mater. Sci. Technol.* **2020**, *53*, 66−72.

(9) Varma, S. K.; Sanchez, F.; Moncayo, S.; Ramana, C. V. Static and cyclic oxidation of Nb-Cr-V-W-Ta high entropy alloy in air from 600 to 1400 °C. *J. Mater. Sci. Technol.* **2020**, *38*, 189−196.

(10) George, E. P.; Raabe, D.; Ritchie, R. O. High-entropy alloys. *Nat. Rev. Mater.* **2019**, *4*, 515−534.

(11) Sun, Y.; Dai, S. High-entropy materials for catalysis: A new frontier. *Sci. Adv.* **2021**, *7*, No. eabg1600.
(12) Tsai, M.-H.; Yeh, J.-W. High-Entropy Alloys: A Critical Review. *Mater. Res. Lett.* **2014**, *2*, 107−123.
(13) Meghwal, A.; Anupam, A.; Murty, B. S.; Berndt, C. C.; Kottada, R. S.; Ang, A. S. M. Thermal Spray High-Entropy Alloy Coatings: A Review. *J. Therm. Spray Technol.* **2020**, *29*, 857−893.
(14) Osei-Agyemang, E.; Balasubramanian, G. Surface oxidation mechanism of a refractory high-entropy alloy. *npj Mater. Degrad.* **2019**, *3*, 20.
(15) Li, W.; Liu, P.; Liaw, P. K. Microstructures and properties of high-entropy alloy films and coatings: a review. *Mater. Res. Lett.* **2018**, *6*, 199−229.
(16) Ye, Y. F.; Wang, Q.; Lu, J.; Liu, C. T.; Yang, Y. High-entropy alloy: challenges and prospects. *Mater. Today* **2016**, *19*, 349−362.
(17) Miracle, D. B.; Senkov, O. N. A critical review of high entropy alloys and related concepts. *Acta Mater.* **2017**, *122*, 448−511.
(18) Dippo, O. F.; Mesgarzadeh, N.; Harrington, T. J.; Schrader, G. D.; Vecchio, K. S. Bulk high-entropy nitrides and carbonitrides. *Sci. Rep.* **2020**, *10*, 21288.
(19) Shu, R.; Lundin, D.; Xin, B.; Sortica, M. A.; Primetzhofer, D.; Magnuson, M.; le Febvrier, A.; Eklund, P. Influence of Metal Substitution and Ion Energy on Microstructure Evolution of High-Entropy Nitride (TiZrTaMe)N_{1-x} (Me = Hf, Nb, Mo, or Cr) Films. *ACS Appl. Electron. Mater.* **2021**, *3*, 2748−2756.
(20) Wu, D.; Kusada, K.; Nanba, Y.; Koyama, M.; Yamamoto, T.; Toriyama, T.; Matsumura, S.; Seo, O.; Gueye, I.; Kim, J.; et al. Noble-Metal High-Entropy-Alloy Nanoparticles: Atomic-Level Insight into the Electronic Structure. *J. Am. Chem. Soc.* **2022**, *144*, 3365−3369.
(21) Gao, S.; Hao, S.; Huang, Z.; Yuan, Y.; Han, S.; Lei, L.; Zhang, X.; Shahbazian-Yassar, R.; Lu, J. Synthesis of high-entropy alloy nanoparticles on supports by the fast moving bed pyrolysis. *Nat. Commun.* **2020**, *11*, 2016.
(22) Qiao, H.; Saray, M. T.; Wang, X.; Xu, S.; Chen, G.; Huang, Z.; Chen, C.; Zhong, G.; Dong, Q.; Hong, M.; et al. Scalable Synthesis of High Entropy Alloy Nanoparticles by Microwave Heating. *ACS Nano* **2021**, *15*, 14928−14937.
(23) Xu, X.; Guo, Y.; Bloom, B. P.; Wei, J.; Li, H.; Li, H.; Du, Y.; Zeng, Z.; Li, L.; Waldeck, D. H. Elemental Core Level Shift in High Entropy Alloy Nanoparticles via X-ray Photoelectron Spectroscopy Analysis and First-Principles Calculation. *ACS Nano* **2020**, *14*, 17704−17712.
(24) Zou, Y.; Wheeler, J. M.; Ma, H.; Okle, P.; Spolenak, R. Nanocrystalline High-Entropy Alloys: A New Paradigm in High-Temperature Strength and Stability. *Nano Lett.* **2017**, *17*, 1569−1574.
(25) Senkov, O. N.; Scott, J. M.; Senkova, S. V.; Miracle, D. B.; Woodward, C. F. Microstructure and room temperature properties of a high-entropy TaNbHfZrTi alloy. *J. Alloys Compd.* **2011**, *509*, 6043−6048.
(26) Senkov, O. N.; Woodward, C. F. Microstructure and properties of a refractory $NbCrMo_{0.5}Ta_{0.5}TiZr$ alloy. *Mater. Sci. Eng. A* **2011**, *529*, 311−320.
(27) Senkov, O. N.; Wilks, G. B.; Scott, J. M.; Miracle, D. B. Mechanical properties of $Nb_{25}Mo_{25}Ta_{25}W_{25}$ and $V_{20}Nb_{20}Mo_{20}Ta_{20}W_{20}$ refractory high entropy alloys. *Intermetallics* **2011**, *19*, 698−706.
(28) Ramana, C. V.; Makeswaran, N.; Zade, V.; Das, D.; Tan, S.; Xu, S.; Beyerlein, I. J. Fabrication and Characterization of High-Quality Epitaxial Nanocolumnar Niobium Films with Abrupt Interfaces on YSZ(001). *J. Phys. Chem. C* **2022**, *126*, 2098−2107.
(29) Makeswaran, N.; Das, D.; Zade, V.; Gaurav, P.; Shutthanandan, V.; Tan, S.; Ramana, C. V. Size- and Phase-Controlled Nanometer-Thick β-Ga_2O_3 Films with Green Photoluminescence for Optoelectronic Applications. *ACS Appl. Nano Mater.* **2021**, *4*, 3331−3338.
(30) Gutierrez, G.; Sundin, E. M.; Nalam, P. G.; Zade, V.; Romero, R.; Nair, A. N.; Sreenivasan, S.; Das, D.; Li, C.; Ramana, C. V. Interfacial Phase Modulation-Induced Structural Distortion, Band Gap Reduction, and Nonlinear Optical Activity in Tin-Incorporated Ga_2O_3. *J. Phys. Chem. C* **2021**, *125*, 20468−20481.
(31) Getahun, Y. W.; Gardea-Torresdey, J.; Manciu, F. S.; Li, X.; El-Gendy, A. A. Green synthesized superparamagnetic iron oxide nanoparticles for water treatment with alternative recyclability. *J. Mol. Liq.* **2022**, *356*, 118983.
(32) Senkov, O. N.; Senkova, S. V.; Woodward, C.; Miracle, D. B. Low-density, refractory multi-principal element alloys of the Cr−Nb−Ti−V−Zr system: Microstructure and phase analysis. *Acta Mater.* **2013**, *61*, 1545−1557.
(33) El-Gendy, A. A.; Khavrus, V. O.; Hampel, S.; Leonhardt, A.; Büchner, B. B.; Klingeler, R. Morphology, Structural Control, and Magnetic Properties of Carbon-Coated Nanoscaled NiRu Alloys. *J. Phys. Chem. C* **2010**, *114*, 10745−10749.
(34) Dunlop, D. J.; Özdemir, Ö. *Rock Magnetism: Fundamentals and Frontiers*; Cambridge University Press: Cambridge, 2001.

https://doi.org/10.1021/acs.jpcc.2c03111
J. Phys. Chem. C 2022, 126, 14255−14263